

Modeling, construction and experimental validation of actuated rolling dynamics of the cylindrical Transforming Roving-Rolling Explorer (TRREx)

L. Edwin, A. Mazzoleni*, T. Gemmer, S. Ferguson

Department of Mechanical and Aerospace Engineering, North Carolina State University, Raleigh, NC 27695, United States

ABSTRACT

Planetary surface exploration technology over the past few years has seen significant advancements on multiple fronts. Robotic exploration platforms are becoming more sophisticated and capable of embarking on more challenging missions. More unconventional designs, particularly transforming architectures that have multiple modes of locomotion, are being studied. This work explores the capabilities of one such novel transforming rover called the *Transforming Roving-Rolling Explorer (TRREx)*. Biologically inspired by the armadillo and the golden-wheel spider, the TRREx has two modes of locomotion: it can traverse on six wheels like a conventional rover on benign terrain, but can transform into a sphere when necessary to negotiate steep rugged slopes. The ability to self-propel in the spherical configuration, even in the absence of a negative gradient, increases the TRREx's versatility and its concept value. This paper describes construction and testing of a prototype cylindrical TRREx that demonstrates that “actuated rolling” can be achieved, and also presents a dynamic model of this prototype version of the TRREx that can be used to investigate the feasibility and value of such self-propelled locomotion. Finally, we present results that validate our dynamic model by comparing results from computer simulations made using the dynamic model to experimental results acquired from test runs using the prototype.

1. Introduction and background

For the last half century there has been growing interest in the exploration of extra-terrestrial planetary surfaces in our solar-system, particularly the terrain of our closest Earth-like neighbor, Mars. The scientific goals that drive these various missions are diverse, but the underlying theme is to search for evidence of past or present life and assess the potential to harbor future human life [1]. Over the past decades, precursor missions have been using robotic exploration platforms to survey the extraterrestrial environment and gather critical data that could serve in the design of future manned missions.

Although there have been a wide variety of vehicle architectures proposed in the literature for use in such precursor missions, all surface exploration platforms sent to Mars thus far have used traditional wheeled locomotion coupled with a particular passive suspension architecture called the “rocker-bogie suspension” [2–5], with the latest addition to the list being NASA's MSL rover [6]. While these traditional rovers are energy efficient and reasonably simple in design, they are significantly limited with respect to the types of terrain that they can safely navigate. In addition to traction issues on slopes [7], traditional wheeled rovers also face the risk of toppling over on steep

slopes. The maximum tilt in any direction that the current Mars rovers can supposedly withstand without toppling over is estimated to be 45degrees [3].

Thus, while traditional wheeled exploration platforms can navigate moderately rough and flat terrain quite efficiently, they are not designed to traverse rugged terrain with steep slopes (see Fig. 1 – Source: ESA webpage [8]). The fact is, however, that most scientifically interesting missions require exploration platforms with capabilities of navigating such types of chaotic terrain. The science strategy for human exploration of Mars [1] identifies the area in Fig. 2 as one that will yield the most scientifically valuable information. This area includes some of the most chaotic terrain features on the planet. It includes the Tharsis volcanoes, the Valles Marineris, and numerous craters and channels.

This desire to explore this particular region of Mars motivates the development of new kinds of rovers that take advantage of the latest advances in robotic technologies to traverse rugged terrain efficiently. This paper presents analysis of one such proposed rover concept called the Transforming Roving-Rolling Explorer (TRREx) [9] that is intended to be able to safely navigate terrains that are combinations of flat areas, gentle gradients, and steep rugged slopes.

* Corresponding author.

E-mail address: a_mazzoleni@ncsu.edu (A. Mazzoleni).

Nomenclature

B	Center of mass of the chassis	$\vec{h}_{B, \text{chassis}}$	Angular momentum of the chassis about B with respect to the inertial frame
\bar{B}	B reference frame	$\vec{h}_{B, \text{sys}}$	Angular momentum of the system about B with respect to the inertial frame
C_j	Center of mass of j th leg, where j is the index for leg number	$\vec{h}_{B, \text{leg}(j)}$	Angular momentum of the j th leg about B with respect to the inertial frame
\bar{C}_j	C_j reference frame, where j is the index for leg number	$\vec{h}_{C_j, \text{leg}(j)}$	Angular momentum of the j th leg about its center of mass C_j
C_{rr}	Coefficient of rolling resistance	R_{ω}	Outer radius of the Planar TRREx
\bar{C}_{rr}	Modified rolling resistance that includes a hyperbolic tangent function	$\vec{r}_{P/B}$	Vector from center of mass of chassis B to point of contact on ground P
\vec{F}_N	Normal reaction force	$\vec{r}_{C_j/B}$	Vector from the center of mass of the chassis to the center of mass of the j th leg.
\vec{F}_{fr}	Frictional reaction force	t	time
\vec{F}_R	Rolling resistance	β	Slope of terrain
\vec{g}	Gravity vector	$\gamma_j, \dot{\gamma}_j, \ddot{\gamma}_j$	Angular displacement, velocity and acceleration of axis $\hat{i}_{\bar{C}_j}$ with respect to axis $\hat{i}_{\bar{B}}$
h_1, h_2	x and y components of the location of the hinge of leg 1 in the frame of the chassis B	μ_s	Coefficient of static friction
$I_{x\bar{B}}, I_{y\bar{B}}, I_{z\bar{B}}$	Principle moments of inertia of the chassis	$\omega_{x\bar{B}}, \omega_{y\bar{B}}, \omega_{z\bar{B}}$	Scalar angular velocities of the chassis about the unit axes of the \bar{B} frame
$I_{x\bar{C}_j}, I_{y\bar{C}_j}, I_{z\bar{C}_j}$	Principle moments of inertia of j th leg	$\omega_{x\bar{C}_j}, \omega_{y\bar{C}_j}, \omega_{z\bar{C}_j}$	Scalar angular velocities of the j th leg about the unit axes of the \bar{C}_j frame
$\hat{i}_{\bar{O}}, \hat{j}_{\bar{O}}, \hat{k}_{\bar{O}}$	Unit axes of an inertial reference frame	$\vec{\omega}_{\bar{O}}^{\bar{B}}$	Vector angular velocity of \bar{B} frame with respect to the \bar{O} frame
$\hat{i}_{\bar{B}}, \hat{j}_{\bar{B}}, \hat{k}_{\bar{B}}$	Unit axes of frame embedded in chassis (chosen to be the principle axes of the chassis)	$\vec{\omega}_{\bar{O}}^{\bar{C}_j}$	Vector angular velocity of \bar{C}_j frame with respect to the \bar{O} frame
$\hat{i}_{\bar{C}_j}, \hat{j}_{\bar{C}_j}, \hat{k}_{\bar{C}_j}$	Unit axes of frame embedded in j th leg (chosen to be the principle axes of each leg)	θ	Angular displacement of axis $\hat{i}_{\bar{B}}$ with respect to $\hat{i}_{\bar{O}}$
l_x, l_y	x and y components of the location of the hinge in the frame of the j th leg C_j	$\dot{\theta} = \omega_{z\bar{B}}$	Angular velocity of the chassis about the $\hat{k}_{\bar{B}}$ axis (or $\hat{k}_{\bar{O}}$ axis)
M	Mass of Chassis	$\ddot{\theta} = \omega_{z\bar{B}}$	Angular acceleration of the chassis about the $\hat{k}_{\bar{B}}$ axis (or $\hat{k}_{\bar{O}}$ axis)
m_L	Mass of each leg	θ_{Oj}, θ_{Cj}	Angular positions of chassis for opening and closing the j th leg
O	Origin of inertial reference frame	Ω_L	Limiting angular velocity magnitude for dynamic ranges in controller
\bar{O}	Inertial reference frame	$(\vec{T}_{B, \text{sys}})_{\text{ext}}$	Total external torque about B acting on the system
$\frac{d}{dt}(\vec{r})$	Time derivative of vector \vec{r} with respect to the \bar{O} frame	$\sum \vec{F}_{\text{ext}}$	Sum of external forces acting on the system
$\vec{v}_{B/O} = \frac{d}{dt}(\vec{r}_{B/O})$	Velocity of point B with respect to the \bar{O} frame		
$\vec{v}_{C_j/O}$	Velocity of point C_j with respect to the \bar{O} frame		
$\vec{v}_{C_j/B} = \frac{d}{dt}(\vec{r}_{C_j/B})$	Velocity of center of mass of the j th leg with respect to the \bar{B} frame		
$\vec{a}_{B/O}$	Inertial acceleration of the center of mass of the chassis		
$\vec{a}_{C_j/O}$	Inertial acceleration of the center of mass of the j th leg		

Biologically inspired by the way the armadillo curls up into a ball when threatened, and the golden wheel spider uses the dynamic advantages of a sphere to roll down hills when escaping danger, the TRREx rover can traverse like a traditional 6-wheeled rover over conventional terrain, but can transform itself into a sphere (see Fig. 3), when necessary, to travel down steep inclines, or navigate rough terrain.

Design of an exploration platform involves detailed systems and subsystems level analysis encompassing all aspects of the defined mission. Since the USP (unique selling proposition) of the TRREx is its increased mobility compared to conventional rovers, the study of the mobility of the TRREx is critical to assessing its potential advantage over traditional rocker-bogie rovers for exploring rugged terrain. Initial studies on the TRREx [10,11] have shown that the transforming architecture has significant performance advantages over conventional rocker-bogie rovers, especially when the target terrain has a combination of steep slopes and rugged terrain.

The dynamics of a wheeled rover with passive suspension is a recurring subject in the literature [5,12,13], as are studies on active suspensions, some of which are very general and can be applied to any rover [14–16]. The dynamics of rolling of a TRREx-like architecture, on the other hand, has, to our knowledge, not been examined in the literature. There are studies that investigate the dynamics of self-

propelled spherical rovers [17–26], but the internal workings of each of these rovers are principally very different from those of the TRREx, hence these studies do not contribute to understanding the rolling dynamics of the TRREx. For this reason, and also for the fact that the overall increased mobility of the TRREx is expected to be attributed to the novel (self-propelled) rolling mode, a detailed study of dynamics of the TRREx in rolling mode has been prioritized and is the subject of this paper.

In the broader framework, this work presents an investigation of the contribution of the rolling mode to the enhanced mobility of the TRREx by studying the Dynamics and Controls problems posed during rolling. Topics such as structural design and power consumption are not considered in this paper, as it is the intent of the current study to highlight the mobility capabilities of the TRREx.

Developing a dynamic model for the spherical TRREx in its rolling mode is complicated and presents a difficult starting point. Therefore, a simplified cylindrical (planar) version of the TRREx is first considered. We note that although the dynamics of a cylindrical TRREx are simpler than those of a spherical TRREx, such a study is an important first step, as valuable insight regarding the mobility of the TRREx in rolling mode can be gained by considering the cylindrical (planar) problem.

In addition to developing a dynamic model of actuated rolling of a cylindrical version of the TRREx, the construction and software

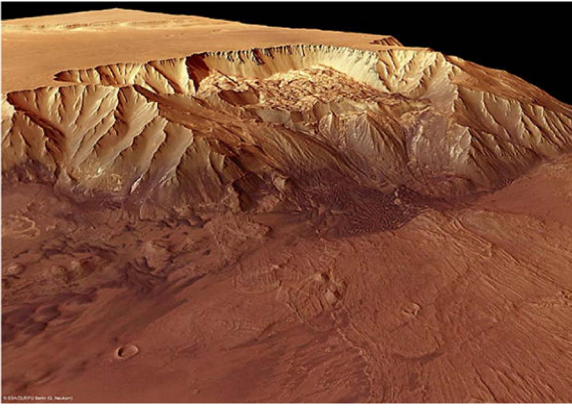


Fig. 1. Terrain features on Mars.
Source: ESA.

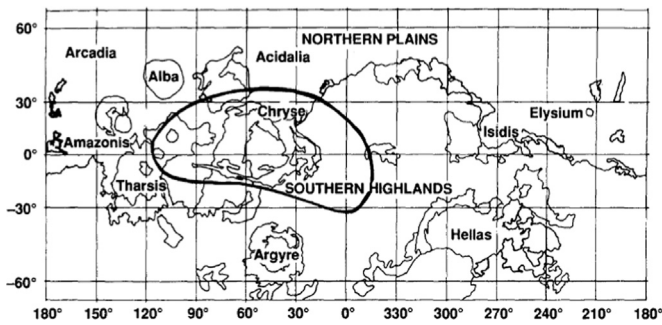


Fig. 2. Proposed region for maximum scientific return [1].



Fig. 3. Transformation of the TRREx between roving and rolling modes.

development of a cylindrical TRREx prototype that is capable of demonstrating actuated rolling is also presented in this paper. Further, in this paper we present a validation of the dynamic model by comparing simulation results with experimental data obtained from test runs conducted using the prototype (Fig. 9).

2. Modeling

Multi-body dynamical systems have been traditionally modeled using various analytical techniques, all of which incorporate some form of rigid constraints to facilitate an order-reduction process that reduces the overall number of independent degrees of freedom, and thus the number of equations required to completely describe the system. This process forces the complexity into a smaller set of equations that can then be integrated to give the time response of the system. Typical examples of such analytical techniques are the Newton-Euler formulation and the use of Lagrange's Equations [27,28]. For this paper, we have employed a Newton-Euler approach to generate our results, as will be described below.

2.1. System description

The cylindrical version of the TRREx (Solidworks® model shown in Fig. 4) has four arms that are actuated by motors. In dynamically modeling this system we consider it to be a multi-body system with 5 bodies; one central frame or 'chassis' and four 'legs'. The four contacts between the legs and chassis are constrained to be hinges with a single rotational degree of freedom. A no-slip condition is assumed at the contact between the ground and the cylindrical surface, and this assumption is checked and verified as part of the simulation (making use of the coefficient of static friction, as listed in Tables 2, 3). Each unconstrained body in the planar space has three independent degrees of freedom, but after applying the rigid constraints at the joint and applying the no-slip constraint, we have from the Kutzbach-Gruebler's mobility equation [36] that such a system has five degrees of freedom. Out of these five degrees of freedom, four degrees of freedom, i.e. the motion of the legs, are control inputs provided by the controller; so in actuality the system has one degree of freedom, namely the angular position of the chassis. The analytical derivation of the governing equation for this degree of freedom is presented below. The development presented assumes that there is no slipping between the ground and the cylindrical surface (as discussed above), and assumes that the movements of the parts of the motor used to rotate the legs contribute a negligible amount to the overall dynamics of the system (due to the relatively small inertias of the moving motor components when compared with the rest of the prototype).

2.2. Definition of frames

The first step in the dynamical analysis of a system of rigid bodies is to define frames, each specified by its origin, unit axes, and the body that it moves with (i.e. is embedded in). For each body that is moving, a separate frame is defined with its origin at the center of mass of that body, with the unit axes aligned in the direction of that body's principle axes. As shown in Fig. 5, if the point B is the center of mass of the chassis (excluding the legs) and the directions \hat{i}_B , \hat{j}_B and \hat{k}_B (\hat{k}_B is into the plane of the paper) are the principle axes directions of the chassis, then the B frame, denoted by \bar{B} , is defined to be a frame with its origin at B and unit axes \hat{i}_B , \hat{j}_B and \hat{k}_B .

In a similar fashion, let the legs be numbered 1 through 4 and have centers of masses C_1 through C_4 respectively. Let the principle axes directions of legs 1 through 4 be \hat{i}_{C_1} , \hat{j}_{C_1} , \hat{k}_{C_1} through \hat{i}_{C_4} , \hat{j}_{C_4} , \hat{k}_{C_4} respectively. Then, \bar{C}_j is defined as a frame with its origin at C_j and unit axes \hat{i}_{C_j} , \hat{j}_{C_j} and \hat{k}_{C_j} for $j=1$ to 4. In addition to these frames, an inertial fixed reference frame \bar{O} is defined, whose origin is arbitrarily placed at the point of contact between the sphere at the ground at a given instant of time (e.g. $t=0$), and whose axes are aligned as shown in Fig. 5.

2.3. Derivation of the governing equation

Following a standard Newton-Euler approach (e.g. as described in Meirovitch [27]), the total external torque about B acting on the system

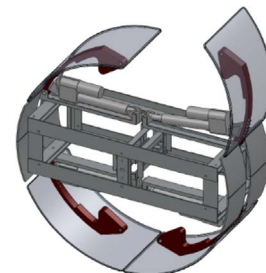


Fig. 4. Cylindrical/Planar TRREx.

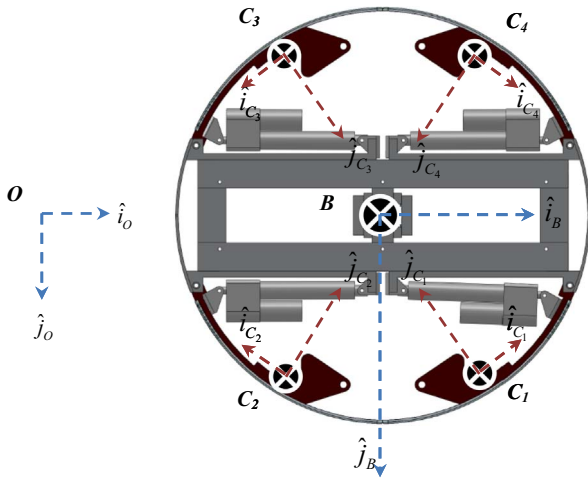


Fig. 5. Definition of Frames.

$(\vec{T}_{B,sys})_{ext}$ is related to the change in angular momentum of the system about B as follows:

$$(\vec{T}_{B,sys})_{ext} = \frac{d}{dt} \left(\vec{h}_{B,sys} \right) + \vec{v}_{B/O} \times m_L \sum_{j=1}^4 \vec{v}_{C_j/O} \quad (1)$$

In this equation, $\vec{h}_{B,sys}$ is the angular momentum of the system about B with respect to the inertial frame, m_L is the mass of each leg, $\vec{v}_{B/O}$ is the inertial velocity of the center of mass of the chassis and $\vec{v}_{C_j/O}$ is the inertial velocity of the center of mass of the j th leg. The term $\vec{v}_{B/O} \times m_L \sum_{j=1}^4 \vec{v}_{C_j/O}$ appears because the torques and angular momentum are written about a point B which is not necessarily the center of mass of the entire system [27].

Next, in Eq. (1), the external torques acting on the system are written in terms of the forces they are derived from, and the right hand side is written in terms of inertias, angular velocities and correction terms (which arise due to the fact that B is not the center of mass of the entire system, as discussed above). The external forces acting on the system are forces due to gravity (vector denoted by \vec{g}) and interaction forces between the ground and the cylindrical surface of the prototype. The ground is modeled as flat terrain (although it can be sloped with respect to the horizontal), and \vec{F}_N is the normal reaction, \vec{F}_{fr} is the frictional reaction and \vec{F}_R is the rolling resistance. These forces are illustrated in Fig. 6, where for ease of illustration the terrain is portrayed as horizontal.

The sum of external torques about B acting on the system is:

$$(\vec{T}_{B,sys})_{ext} = \vec{r}_{P/B} \times (\vec{F}_{fr} + \vec{F}_N) + m_L \sum_{j=1}^4 \left(\vec{r}_{C_j/B} \times \vec{g} \right) \quad (2)$$

where $\vec{r}_{P/B}$ is a vector pointing from the center of mass of the chassis B to the point of contact with the ground, P , and $\vec{r}_{C_j/B}$ is the vector from the center of mass of the chassis B to the center of mass of the j th leg (i.e. the point C_j). Since the system consists of the chassis and the four legs (we are considering the angular momentum contributions of the other components to be negligible in comparison), the total angular momentum of the system can be written as

$$\vec{h}_{B,sys} = \vec{h}_{B,chassis} + \sum_{j=1}^4 \vec{h}_{B,leg(j)}$$

where $\vec{h}_{B,chassis}$ is the angular momentum of the chassis about B with respect to the inertial frame and $\vec{h}_{B,leg(j)}$ is the angular momentum of the j th leg about B with respect to the inertial frame.

It can be shown [27] that the angular momentum of a body about a

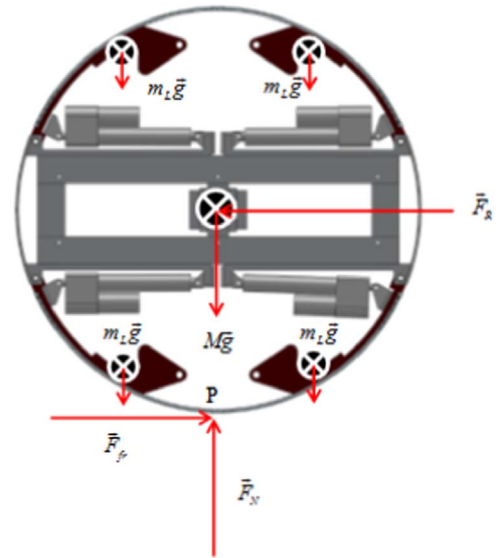


Fig. 6. External forces on the Cylindrical TRREx.

point other than its center of mass can be written as a function of its velocity and its angular momentum about its center of mass. Therefore, following [27] we have that the angular momentum of each leg about point B can be expressed as follows:

$$\vec{h}_{B,leg(j)} = \vec{h}_{C_j,leg(j)} + \vec{r}_{C_j/B} \times m_L \vec{v}_{C_j/O}$$

Therefore,

$$\vec{h}_{B,sys} = \vec{h}_{B,chassis} + \sum_{j=1}^4 \left(\vec{h}_{C_j,leg(j)} + \vec{r}_{C_j/B} \times m_L \vec{v}_{C_j/O} \right) \quad (3)$$

where $\vec{h}_{C_j,leg(j)}$ is the angular momentum of the j th leg about its center of mass C_j .

If the moments of inertia of a body are computed about its principle axes, then the products of inertia will be zero. For the chassis, its reference frame axes \hat{i}_B , \hat{j}_B and \hat{k}_B were by definition chosen to be the principal axes, thus let the principle inertia components computed about these axes be I_{x_B} , I_{y_B} , I_{z_B} , respectively. Writing the angular velocity of the \bar{B} frame with respect to the \bar{O} frame as $\vec{\omega}_{\bar{B}} = \omega_{x_B} \hat{i}_B + \omega_{y_B} \hat{j}_B + \omega_{z_B} \hat{k}_B$, it can be shown [27] that $\vec{h}_{B,chassis} = I_{x_B} \omega_{x_B} \hat{i}_B + I_{y_B} \omega_{y_B} \hat{j}_B + I_{z_B} \omega_{z_B} \hat{k}_B$ since B is the center of mass of the chassis. Similarly, if for each leg $I_{x_{C_j}}$, $I_{y_{C_j}}$, $I_{z_{C_j}}$ are defined to be the inertia components about the principle axes \hat{i}_{C_j} , \hat{j}_{C_j} , \hat{k}_{C_j} , respectively, and the angular velocity of the \bar{C}_j frame with respect to the \bar{O} frame is $\vec{\omega}_{\bar{C}_j} = \omega_{x_{C_j}} \hat{i}_{C_j} + \omega_{y_{C_j}} \hat{j}_{C_j} + \omega_{z_{C_j}} \hat{k}_{C_j}$, then it can be shown [27] that $\vec{h}_{C_j,leg(j)} = I_{x_{C_j}} \omega_{x_{C_j}} \hat{i}_{C_j} + I_{y_{C_j}} \omega_{y_{C_j}} \hat{j}_{C_j} + I_{z_{C_j}} \omega_{z_{C_j}} \hat{k}_{C_j}$.

Differentiating Eq. (3) with respect to the \bar{O} frame yields Eq. (4),

$$\begin{aligned} \frac{d}{dt} \left(\vec{h}_{B,sys} \right) &= \frac{d}{dt} \left(\vec{h}_{B,chassis} \right) + \sum_{j=1}^4 \left(\frac{d}{dt} \left(\vec{h}_{C_j,leg(j)} \right) \right) \\ &\quad + \frac{d}{dt} \left(\vec{r}_{C_j/B} \times m_L \vec{v}_{C_j/O} \right) \end{aligned} \quad (4)$$

Rewriting the first term on the right hand side by using the transport theorem [28] we obtain:

$$\begin{aligned} \frac{\bar{d}}{dt} \left(\bar{\vec{h}}_{B, \text{chassis}} \right) &= \frac{\bar{B}}{dt} \left(\bar{\vec{h}}_{B, \text{chassis}} \right) + \bar{\vec{\omega}}_{\bar{B}} \times \bar{\vec{h}}_{B, \text{chassis}} \\ &= (I_{x\bar{B}} \dot{\omega}_{x\bar{B}} - (I_{y\bar{B}} - I_{z\bar{B}}) \omega_{y\bar{B}} \omega_{z\bar{B}}) \hat{i}_{\bar{B}} \\ &\quad + (I_{y\bar{B}} \dot{\omega}_{y\bar{B}} - (I_{z\bar{B}} - I_{x\bar{B}}) \omega_{x\bar{B}} \omega_{z\bar{B}}) \hat{j}_{\bar{B}} \\ &\quad + (I_{z\bar{B}} \dot{\omega}_{z\bar{B}} - (I_{x\bar{B}} - I_{y\bar{B}}) \omega_{x\bar{B}} \omega_{y\bar{B}}) \hat{k}_{\bar{B}} \end{aligned}$$

Since our system is restricted to planar motion about the $\hat{k}_{\bar{B}}$ axis, we have $\dot{\omega}_{x\bar{B}} = \dot{\omega}_{y\bar{B}} = \dot{\omega}_{z\bar{B}} = \dot{\omega}_{y\bar{B}} = 0$. Thus, the above expression reduces to,

$$\frac{\bar{d}}{dt} \left(\bar{\vec{h}}_{B, \text{chassis}} \right) = I_{z\bar{B}} \dot{\omega}_{z\bar{B}} \hat{k}_{\bar{B}} \quad (5)$$

Following a similar process for each leg, we obtain,

$$\frac{\bar{d}}{dt} \left(\bar{\vec{h}}_{C_j, \text{leg}(j)} \right) = I_{z\bar{C}_j} \dot{\omega}_{z\bar{C}_j} \hat{k}_{\bar{C}_j} \quad (6)$$

Using the product rule and transport theorem [28] the second term in the summation in (4) can be re-written as:

$$\begin{aligned} \frac{\bar{d}}{dt} \left(\bar{\vec{r}}_{C_j/B} \times m_L \bar{\vec{v}}_{C_j/O} \right) &= m_L \left(\bar{\vec{v}}_{C_j/B} \times \bar{\vec{v}}_{C_j/O} + (\bar{\vec{\omega}}_{\bar{B}} \times \bar{\vec{r}}_{C_j/B}) \times \bar{\vec{v}}_{C_j/O} \right. \\ &\quad \left. + \bar{\vec{r}}_{C_j/B} \times \bar{\vec{a}}_{C_j/O} \right) \end{aligned} \quad (7)$$

where $\bar{\vec{v}}_{C_j/B} = \frac{\bar{B}}{dt} \left(\bar{\vec{r}}_{C_j/B} \right)$ is the velocity of center of mass of the j^{th} leg with respect to the \bar{B} frame and $\bar{\vec{a}}_{C_j/O}$ is the inertial acceleration of the center of mass of the j^{th} leg.

Substituting Eqs. (5–7) into Eq. (4) gives:

$$\begin{aligned} \frac{\bar{d}}{dt} \left(\bar{\vec{h}}_{B, \text{sys}} \right) &= I_{z\bar{B}} \dot{\omega}_{z\bar{B}} \hat{k}_{\bar{B}} + \sum_{j=1}^4 I_{z\bar{C}_j} \dot{\omega}_{z\bar{C}_j} \hat{k}_{\bar{C}_j} \\ &+ m_L \sum_{j=1}^4 \left(\bar{\vec{v}}_{C_j/B} \times \bar{\vec{v}}_{C_j/O} + (\bar{\vec{\omega}}_{\bar{B}} \times \bar{\vec{r}}_{C_j/B}) \times \bar{\vec{v}}_{C_j/O} + \bar{\vec{r}}_{C_j/B} \times \bar{\vec{a}}_{C_j/O} \right) \end{aligned} \quad (8)$$

Now, substituting Eqs. (2) and (8) into Eq. (1), we obtain:

$$\begin{aligned} \bar{\vec{r}}_{P/B} \times (\bar{\vec{F}}_{fr} + \bar{\vec{F}}_N) + m_L \sum_{j=1}^4 \left(\bar{\vec{r}}_{C_j/B} \times \bar{\vec{g}} \right) &= I_{z\bar{B}} \dot{\omega}_{z\bar{B}} \hat{k}_{\bar{B}} + \sum_{j=1}^4 I_{z\bar{C}_j} \dot{\omega}_{z\bar{C}_j} \hat{k}_{\bar{C}_j} \\ &+ m_L \sum_{j=1}^4 \left(\bar{\vec{v}}_{C_j/B} \times \bar{\vec{v}}_{C_j/O} + (\bar{\vec{\omega}}_{\bar{B}} \times \bar{\vec{r}}_{C_j/B}) \times \bar{\vec{v}}_{C_j/O} + \bar{\vec{r}}_{C_j/B} \times \bar{\vec{a}}_{C_j/O} \right. \\ &\quad \left. + \bar{\vec{v}}_{B/O} \times \bar{\vec{v}}_{C_j/O} \right) \end{aligned} \quad (9)$$

It is now noted that for the planar system $\hat{k}_{\bar{B}} = \hat{k}_{\bar{C}_j} = \hat{k}_{\bar{O}}$, and that the $\hat{k}_{\bar{O}}$ component in the vector Eq. (9) will ultimately yield the equation of motion for the degree of freedom associated with the chassis.

The unknown forces in Eq. (9) can be found when Newton's second law is applied to the system:

$$\sum \bar{\vec{F}}_{ext} = M \bar{\vec{a}}_{B/O} + m_L \sum_{j=1}^4 \bar{\vec{a}}_{C_j/O}$$

In the above equation, $\sum \bar{\vec{F}}_{ext}$ is the sum of external forces acting on the system, M is the mass of the chassis, m_L is the mass of each leg, and $\bar{\vec{a}}_{B/O}$ and $\bar{\vec{a}}_{C_j/O}$ are the inertial accelerations of the center of mass of the chassis and the acceleration of the center of mass of the j^{th} leg, respectively. External forces acting on the system are gravity, static friction, the normal reaction of the ground acting on the rover, and rolling resistance forces. Hence we have:

$$M \bar{\vec{g}} + 4m_L \bar{\vec{g}} + \bar{\vec{F}}_{fr} + \bar{\vec{F}}_N + \bar{\vec{F}}_R = M \bar{\vec{a}}_{B/O} + m_L \sum_{j=1}^4 \bar{\vec{a}}_{C_j/O} \quad (10)$$

Note that rolling resistance is modeled as a force which opposes the translational motion of the rover whose magnitude is proportional to the magnitude of the normal force, i.e.:

$$\begin{aligned} \bar{\vec{F}}_R &= -C_{rr} |\bar{\vec{F}}_N| \hat{i}_{\bar{O}} \quad \text{if motion is in the positive } \hat{i}_{\bar{O}} \text{ direction} \\ \bar{\vec{F}}_R &= C_{rr} |\bar{\vec{F}}_N| \hat{i}_{\bar{O}} \quad \text{if motion is in the negative } \hat{i}_{\bar{O}} \text{ direction} \end{aligned}$$

2.4. Numerically integrating the governing equations

In developing computer code to numerically integrate the analytical equations listed above, the dependence of the direction of rolling resistance force on the direction of motion is implemented by inserting a hyperbolic tangent function in the evaluation of a modified rolling resistance coefficient \bar{C}_{rr} [35]. This was done to avoid the integrator taking inordinate amounts of time to integrate when the velocity of the chassis becomes extremely small (close to zero), and the idea behind this numerical technique is described below. When the system is approaching rest, the direction of the rolling resistance force keeps changing almost every time-step, which can lead to significant numerical errors over time. The hyperbolic tangent function mitigates this issue by providing a margin between a small positive velocity and a small negative velocity during which the opposing force tapers off to zero at zero velocity.

Thus, if $\bar{\vec{F}}_R = -\bar{C}_{rr} |\bar{\vec{F}}_N| \hat{i}_{\bar{O}}$ then \bar{C}_{rr} is set to be: $\bar{C}_{rr} = C_{rr} \tanh\left(\frac{\dot{\theta}}{\theta_{\text{trigger}}}\right)$ where θ_{trigger} is some small positive value of angular velocity. Note that the value of the hyperbolic tangent function rapidly approaches unity when its argument moves away from zero, takes the sign of its argument, (and hence of $\dot{\theta}$), rapidly approaches zero as $\dot{\theta}$ approaches zero, and thus makes the rolling resistance force zero in a continuous fashion as $\dot{\theta}$ approaches zero.

The $\hat{j}_{\bar{O}}$ component in Eq. (10) is used to first solve for the normal force. From this, the rolling resistance can be determined and used in the $\hat{i}_{\bar{O}}$ component to solve for the frictional reaction. This allows for the quantity $(\bar{\vec{F}}_{fr} + \bar{\vec{F}}_N)$ to be solved for in Eq. (10) and plugged into Eq. (9). The $\hat{k}_{\bar{O}}$ component of Eq. (9) is in terms of system geometric and mass constants and the control inputs of the legs, which are all known. The only unknown is the variable describing rotary motion of the chassis about the \bar{B} frame. Labeling this variable as θ , we have that $\omega_{z\bar{B}} = \dot{\theta}$ and $\dot{\omega}_{z\bar{B}} = \ddot{\theta}$. Thus, Eq. (9) yields a second order differential equation in θ that can be numerically integrated to give the motion of the chassis as a function of time.

2.5. Control inputs to model

Recalling Fig. 5, if γ_{jd} is the desired angle at a given instant of time between the $\hat{i}_{\bar{C}_j}$ and $\hat{i}_{\bar{B}}$ axes in the positive $\hat{k}_{\bar{C}_j}$ direction, then the desired input motions of the legs (as functions of time) are given by γ_{jd} , $\dot{\gamma}_{jd}$, $\ddot{\gamma}_{jd}$ for the four legs i.e. $j=1, 2, 3, 4$. When these values are inserted into the equation of motion, the result is a second order differential equation with the only unknown being the chassis angular position θ . This differential equation can be then be numerically integrated (we used the *ode45* suite in MATLAB® [37]) to obtain the time evolution of the chassis angle. When performing the simulations, we assume that the actuators (linear motors) generate the desired motions of the legs (i.e. the γ_{jd} terms as functions of time) exactly, i.e. the motion of the legs are treated as an input to the system when computing the system response.

Initial studies assumed that the angular acceleration of each leg followed a cubic polynomial (in time) from rest position to rest position. But it was observed from experiments using the prototype that a piecewise constant acceleration of the piston (of the linear motor

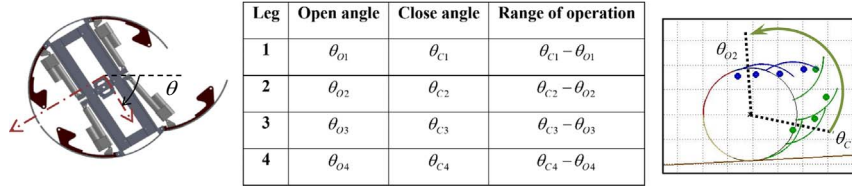


Fig. 7. Controller – Dynamic ranges of operation.

between the leg and the chassis), when transformed to the angle of the leg, better characterized the opening and closing motion of the legs, so this was the approach taken in performing the simulations, as will be seen in later sections of this paper.

One of the intended features of the TRREx is that self-propulsion (actuated rolling) can be achieved by controlling the timing of opening and closing of legs such that continuous rolling is generated, and we will demonstrate that this intended feature is a reality through both analysis and experiment. Note that as the TRREx rolls, the legs will have to be retracted in time so that the system does not roll over an opened leg (i.e. so that ‘ground interference’ does not occur). Each leg could be set to open and close at pre-determined values of the angular position (for range of operation, see Fig. 7), but as the angular velocity increases the legs will have less and less time to completely retract. Thus, the maximum speed of actuated rolling is directly limited by the capacity of the actuators which move the legs; therefore, to avoid ground interference: (1) the actuators are set to retract the legs at maximum capacity; and (2) the ranges of operation are made to be a function of chassis angular velocity, i.e. the controller starts closing the legs earlier and earlier as the speed of rolling increases.

Looking at Fig. 7, we note that if leg 2 is set to open at a particular chassis angle $\theta = \theta_{O2}$ (note that here ‘O’ in the subscript stands for ‘open’), and close at angle $\theta = \theta_{C2}$ (note that here ‘C’ in the subscript stands for ‘closed’), we have that as the angular velocity of the system increases, this closing angle will move closer to θ_{O2} (proportionally) and is equal to θ_{O2} at some limiting angular velocity Ω_L . Therefore the range of operation of the leg decreases linearly and tends to zero as the system velocity tends to the limiting velocity.

Thus, in our closed loop scheme, control inputs to the legs are functions of both of the current states (angular position and velocity). Since the control inputs are discontinuous functions of the states, they are implemented in code by detecting ‘event crossings’ (as opposed to substituting the inputs as a function of states in the equations of motion). During integration of the equation of motion, when an event is detected (i.e. when the chassis position crosses an open or close angle of a leg) the input to the system is changed appropriately and integration is then continued. It should be noted that, upon the occurrence of an event, ranges of all the legs except the one that just finished actuation are updated (this avoids jitter).

3. Construction and development of prototype and microcontroller for Cylindrical TRREx

3.1. Hardware

3.1.1. Structure

A cylindrical prototype of the TRREx was constructed to facilitate the experimental validation of simulation results obtained from the dynamic model. The prototype, as is the multi-body system modeled above, is a 5-body system with a central chassis and four legs hinged to this chassis. The physical prototype differs, however, from the conceptual model seen in Fig. 4 in that the physical prototype rolls on circular disks, rather than on the curved surfaces of its legs (see Fig. 8). This was done to avoid machining curved surface areas; however, given the assumptions made in creating the mathematical model of the conceptual cylindrical TRREx, (i.e. we assumed that the surface of

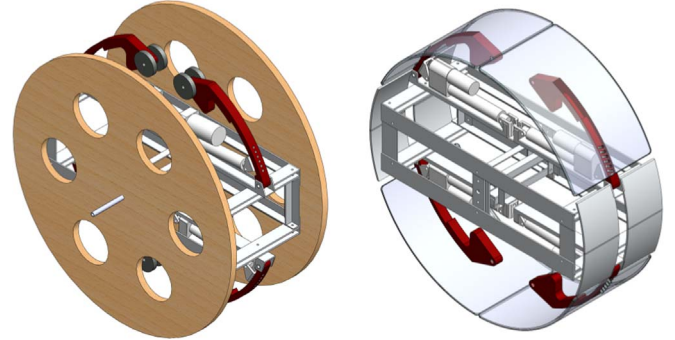


Fig. 8. Prototype (left) in comparison with the dynamically modeled system (right).

Table 1
Physical/ Design parameters of prototype cylindrical TRREx.

Parameters	Description	Symbol	Value	Units
Geometric parameters	Outer radius of cylindrical surface	R_w	0.3937	m
	Location of hinge of leg w.r.t. center of chassis	h_1	0.3364	m
		h_2	0.1259	m
Mass parameters (Leg Design A)	Location of center of mass of leg w.r.t. hinge	l_x	0.1967	m
		l_y	0.0364	m
	Mass of ‘chassis’	M	24	kg
	Mass of each ‘leg’	m_L	0.8720	kg
	Inertia about the rotation axis of chassis	$I_{z\bar{B}}$	1.2650	kg m ²
	Inertia about the rotation axis of each leg	$I_{z\bar{C}_j}$	0.0082	kg m ²

contact is always a continuous circular shape) the equations of motion for the physical prototype will be the same as for the conceptual model after the mass and moment of inertia properties of the disks are incorporated into the mass and moment of inertia properties of the chassis. Hence, both the conceptual and the physical cylindrical TRREx models are completely described by the same set of physical parameters (see Table 1), namely, the outer radius of the cylindrical surface (R_w), the location of the center of mass of the leg with respect to the hinge (l_x and l_y), the location of a hinge with respect to the center of mass of the chassis (h_1 and h_2), the mass of the chassis (M) and each leg (m_L) and the inertia about the axis of rotation of the chassis ($I_{z\bar{B}}$) and each leg ($I_{z\bar{C}_j}$) about the respective points B and C_j .

Also provided for in the physical prototype is the ability to modify the mass properties of the legs between experimental runs by adding lead weights at the ends of the legs (shown as small grey circular disks in Fig. 8). This enables the validation of the results from the dynamic models for different points in the design space.

3.1.2. Electronics

The legs are driven by high speed linear motors with potentiometer feedback and run on a 12 V DC supply (see Fig. 9). They are driven by pulse-width-modulation through an H-bridge. A multi-axis accel-

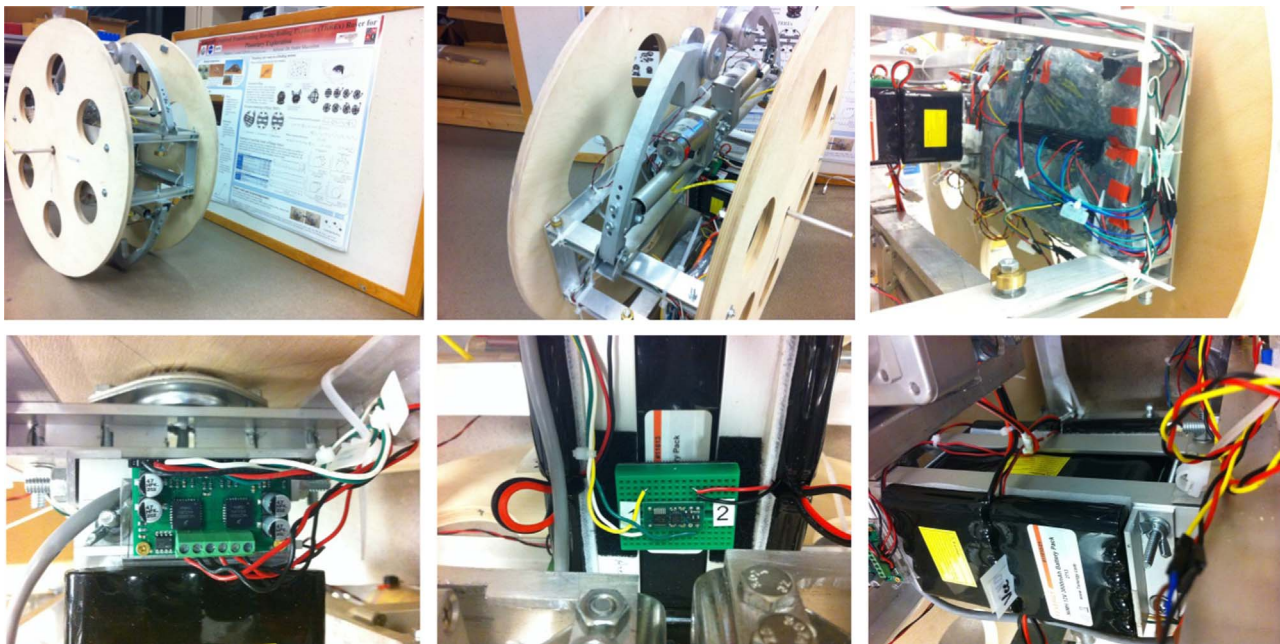


Fig. 9. Prototype and Hardware (Top-left: System, Top-middle: Legs and actuators, Top-right: Controller, Bottom-left: H-bridge, Bottom-middle: Accelerometer, Bottom-right: Battery packs).

ometer is used as an orientation sensor. It determines the gravity vector direction in the chassis frame from which the micro-controller is able to compute the orientation of the chassis. A National Instruments micro-controller, the Sb-RIO 9611 [38] is used to implement the control system. It has a 266 MHz processor running a RTOS (real-time operating system), 128 MB storage, 64 MB RAM and has a 1 M gate Xilinx Spartan FPGA. The board is powered by a 24 V DC supply. There are two battery packs: a 12 V 10,000 mAh battery to run the motors and a 24 V 3800 mAh battery to run the controller. It should be noted that care was taken while mounting all the electronic components to ensure that the center of mass of the entire system when all the legs are closed remained at the center of the chassis.

3.2. Software

The microcontroller can be programmed using the National instruments proprietary graphical programming software known as LabVIEW [39]. The processor onboard runs a RTOS which interacts with the FPGA module which in turn interfaces with hardware I/O. As the role of the microcontroller (target) is to perform simultaneous control and data acquisition while the system is in motion, a ‘headless’ architecture was chosen for the embedded system on the TRREx prototype, i.e. all data acquisition, control and storage is performed on the target and there is no need for interaction with a computer (host). Once the target memory is full, data can be transferred to another storage device using standard FTP protocol over an Ethernet connection.

A headless architecture has two top level ‘Virtual Instruments’ (VI’s) running asynchronously; one on the RTOS and the other on the FPGA. An architecture diagram showing the processes and interconnecting communication paths is depicted in Fig. 10. The Data acquisition loop/process on the FPGA records the values at the analog inputs of the target which are connected to the potentiometers and the accelerometer. This data along with a timestamp generated by the 40 MHz FPGA clock is streamed through a single DMA (dynamic memory allocation) FIFO (first-in-first-out) stream in an interleaved fashion and is unpacked on the data logger process on the Real-time VI (RT VI) using decimation before it is saved onto the onboard memory. Simultaneously this data is also made available to the control loop

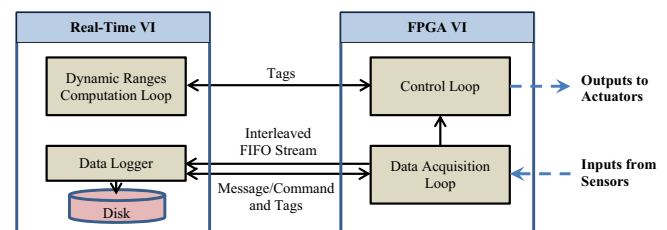


Fig. 10. Embedded system architecture.

process on the FPGA (via inter-process communications), which uses the data to compute the orientation of the chassis and the positions of the legs. This information is shared via current value tags with the Dynamic range computation loop on the RT VI that further computes the rotational velocity of the chassis and the dynamic ranges. This information is again relayed back to the control loop on the FPGA VI (via tags) which then makes control decisions based on the position of the chassis and dynamic ranges of operation of each leg and sends out control signals to the motors.

While in terms of high throughput at high acquisition rates a DMA FIFO stream is the preferred communication path for data transfer in data acquisition processes, to ensure low latency (at high execution rates) in control, current value tags were the preferred communication path between control processes on the RT VI and the FPGA VI (Fig. 11). Messages/Commands were also used to relay infrequent data that facilitate lossless data transfer and storage (acknowledgment flag, buffer overflow flag etc.). The dynamic ranges computation process was offloaded onto the Real-Time processor to take advantage of floating-point math which is more efficiently executed by a processor compared to the FPGA.

Additional logic in the control loop on the FPGA provided for an initiation time for the legs to go to their initial positions (and for filter stabilization), for software implemented limit switches with locking torques to hold the leg in position when fully open or closed and also for hard stops in cases of emergency. The dynamic ranges logic in the RT VI was implemented in exactly the same way as in the mathematical model of the system, i.e. the ranges of operation of each leg get updated (as a function of current rotational velocity) every time an event is detected.

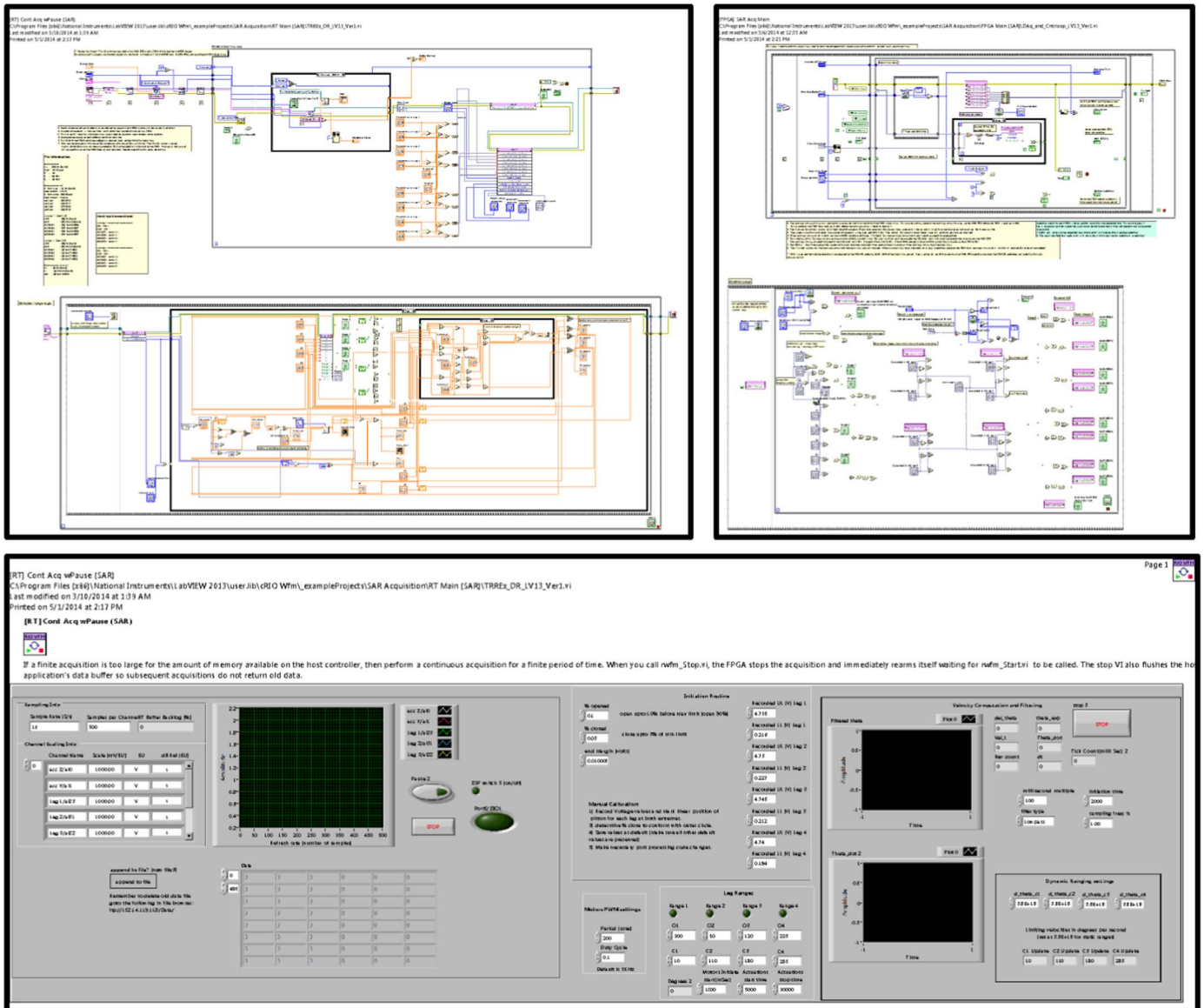


Fig. 11. LabVIEW – Top level VI's and RT VI front panel.

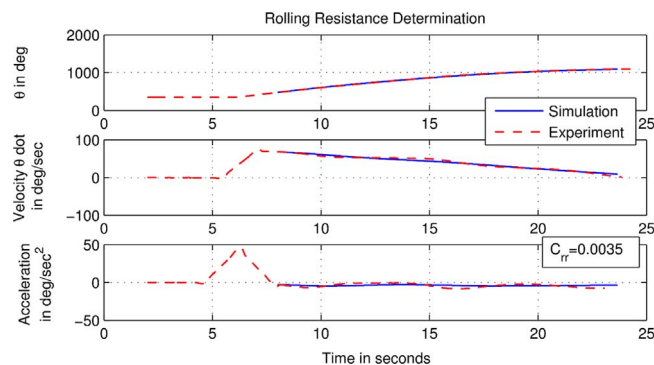


Fig. 12. Rolling resistance determination.

4. Comparison of simulations versus experiments

4.1. Determination of parameters

In order to compare experimental results with the results produced by the mathematical model, the physical parameters (dimensions,

masses and inertias) of the prototype must be determined accurately and input into the model. The geometric and mass properties can be measured directly from the prototype but the inertias were extracted from Solidworks® data. Care was taken to set relatively strict tolerances during the fabrication processes such that the deviation of the mass properties of the parts from the Solidworks® model to the physical prototype were minimal. The physical parameters for the prototype (with 'leg design A') are listed in Table 1 (see Table 4 for information on leg designs 'B' and 'C').

The determination of the coefficient of rolling resistance was done by experimentally measuring the deceleration during a free coast, assuming this to be a constant value, and using the computational model to find the value of rolling resistance that yields this deceleration [40]. We used two different surfaces in our experiments, as is discussed below. Experimental results showing how rolling resistance was calculated for 'Surface 1' are shown in Fig. 12. The sub-plots starting from the top are position, velocity and acceleration, respectively. The system is accelerated to a certain speed and then allowed to freely coast to a halt. In this case a rolling resistance coefficient value of 0.0035 in the analytical model corresponds to the average deceleration experienced by the experimental prototype on this surface. Static friction

Table 2

Environmental parameters for Surface 1.

Parameters	Description	Symbol	Value	Units
Environment parameters	Gravity	g	9.81	m/s ²
	Rolling resistance	C_{rr}	0.0035	–
	Coefficient of static friction	μ_s	0.5	–
	Slope of terrain	β	0	Deg.

Table 3

Environmental parameters for Surface 2.

Parameters	Description	Symbol	Value	Units
Environment parameters	Gravity	g	9.81	m/s ²
	Rolling resistance	C_{rr}	0.0175	–
	Coefficient of static friction	μ_s	0.75	–
	Slope of terrain	β	0	Deg.

Table 4

Leg design parameters.

Parameters	l_x	l_y	m_L	$I_{z\bar{c}_j}$
Units	m	m	kg	kg m ²
Leg Design A	0.1967	0.0364	0.8720	0.0082
Leg Design B	0.2419	0.0500	1.4240	0.0137
Leg Design C	0.2624	0.0529	1.9510	0.0162

values for the testing surfaces are taken from the literature [41–43]. All environmental parameters for ‘Surface 1’ are listed in Table 2.

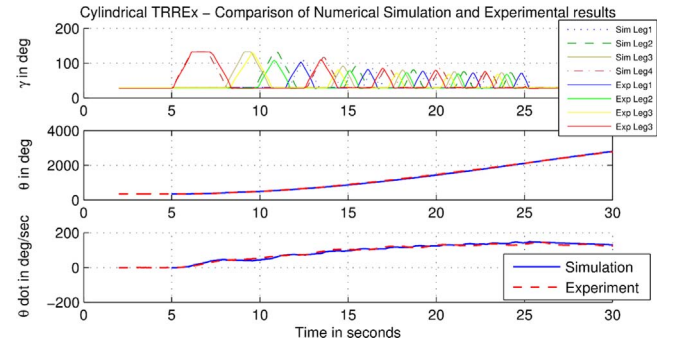
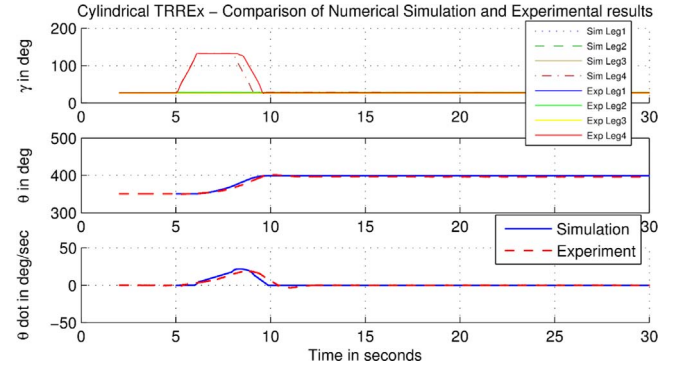
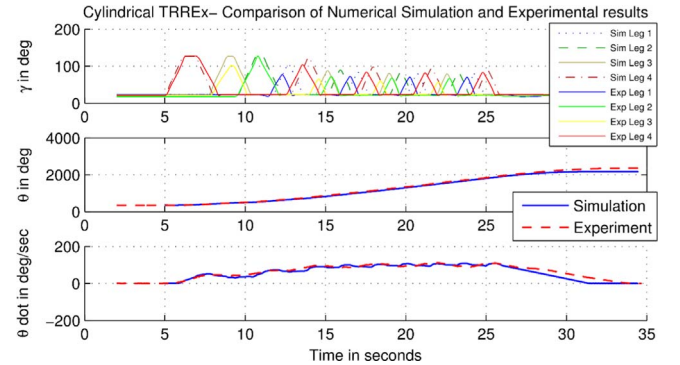
4.2. Comparison of responses

To validate the results from the models, several different cases are presented each representing a different point in the parameter space of the problem. Two different surfaces are considered, ‘Surface 1’, represented by parameters shown in Table 2, was a terrazzo floored hallway, and ‘Surface 2’, represented by parameters shown in Table 3, was a carpeted hallway.

Also, three different mass distributions for the legs were considered (achieved by varying the masses attached to the ends of the legs). The parameters for these, i.e. ‘leg design A’ (extracted from data in Table 1), ‘leg design B’ and ‘leg design C’, are shown in Table 4.

Case 1. Leg Design A on Surface 1.

First, the system with Leg design A was tested by setting its programmable electronics to perform actuated rolling on ‘Surface 1’. Data was acquired using the physical prototype and simulation results were generated for this scenario using the mathematical model. It should be noted that for all the simulations, the ground interaction forces were monitored after the integration and checked to ensure that $|\vec{F}_f| < \mu_s |\vec{F}_N|$ at every time-step, i.e. that slip did not occur during the simulation. The plots in Fig. 13 show the experimental data acquired in comparison with the simulation results. Leg actuations are started at the 5 s mark (true for Cases 2–5, below, as well) and the system performed actuated rolling for 20 s (i.e. actuations were stopped at the 25 s mark). The top subplot shows the leg actuations, the middle subplot shows the chassis position, and the bottom subplot shows the velocity of the chassis with time. It can be seen from this comparative plot that there is good correspondence between experimentally observed data and simulation results with the system using Leg design A while rolling on ‘Surface 1’. (Note that the difference in leg positions versus time between the experiment and the simulation is because of

**Fig. 13.** Experimental Validation - ‘Leg Design A’ on ‘Surface 1’.**Fig. 14.** Experimental Validation - ‘Leg Design A’ on ‘Surface 2’.**Fig. 15.** Experimental Validation - ‘Leg Design B’ on ‘Surface 2’.

the fact that the opening and closing angles of a particular leg (see Fig. 7) were reached at slightly different instances of time in the physical system as compared to the simulation).

Case 2. Leg Design A on Surface 2.

Next, the same system was placed on ‘Surface 2’ which has a higher rolling resistance than ‘Surface 1’. The actuation period was identical to Case 1, and results of both the experiment and simulation are shown in Fig. 14. It is seen in this case that the system starts to roll, but is not able to roll enough for the next leg in sequence to constructively contribute to the perpetuation of rolling motion. Thus the system with this design configuration (Leg design A) experiences ‘stall’ and is not able to achieve a continuous actuated rolling motion on ‘Surface 2’. It can be seen from the comparative plot that this ‘stall’ is also predicted by the simulation.

Case 3. Leg Design B on Surface 2.

In the next case ‘Leg design B’ was mounted on the system and the system was tested on ‘Surface 2’. The actuation period was identical to Case 1, and the results are shown in Fig. 15. Since Leg design B

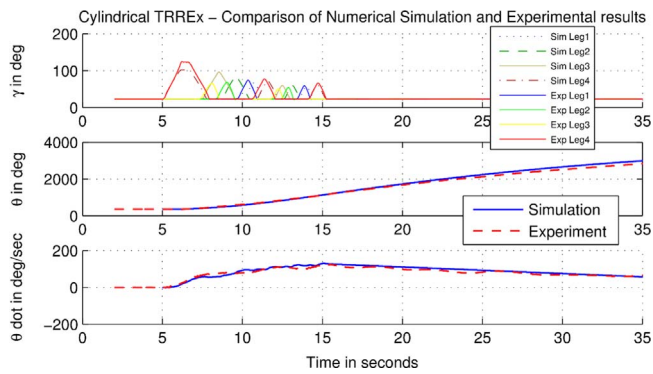


Fig. 16. Experimental Validation - 'Leg Design B' on 'Surface 1' with Dynamic Ranges.

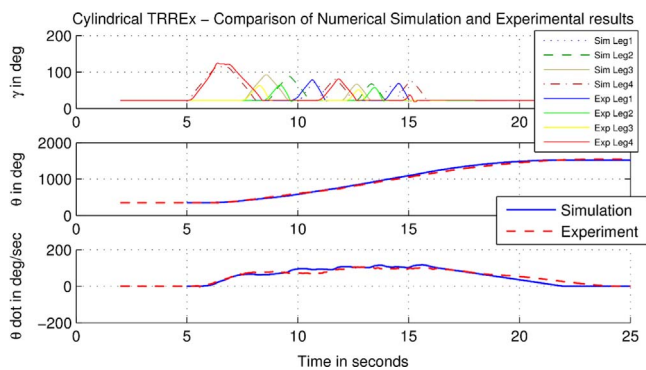


Fig. 17. Experimental validation - 'Leg Design C' on 'Surface 2'.

increases the mass of the leg and moves the center of mass further out compared to Leg design A, we see that the system is now able to achieve continuous actuated rolling without stalling. Again, simulation predictions are consistent with experimental observations.

Case 4. Leg Design B on Surface 1 with Dynamic ranges.

For the next case, the system with Leg design B was tested on 'Surface 1'. Simulations and experiments showed that under this experimental configuration the system tended to reach high rolling velocities quickly, so that the legs could not be retracted in time to avoid the system rolling over an opened leg (i.e. 'ground interference' would occur). To avoid this, dynamic ranges with a limiting velocity of $\Omega_L = 4\pi \text{ rad/sec} = 720^\circ/\text{sec}$ were used (see Section 2.2). (Note that for all previous simulations, i.e. Cases 1–3, static ranges were used, i.e. the range of operation of the legs did not depend on velocity.) Actuated rolling was implemented for 10 s, and then the system was allowed to coast. The comparative results of experimental data and simulation are shown in Fig. 16; note the good agreement between simulation and experiment.

Case 5. Leg Design C on Surface 2.

In this case Leg design C was mounted on the system, which in comparison to Leg design B further increased the mass of the leg and moved the center of mass out towards the tip of the leg. Actuated rolling was implemented (on 'Surface 2') for 10 s and then the system was allowed to coast to a halt. The comparative plots of simulation predictions and experimental data are shown in Fig. 17, and a good correspondence between the two is observed.

By comparing the results at different points in parameter space with multiple experimental runs, and observing that the simulation results match well with the experimental data in all cases, we have shown that our dynamic model of the cylindrical TRREx does a good job of predicting the actual motion of the system. The developed model can thus be used as a design tool and has applications in analysis, design, and control optimization of the system for a given target environment.

For example, some general/characteristic trends were observed as we moved from leg design A to leg design B to leg design C (assuming the same motor capacity), in that we can see that as we increase the mass placed at the end of the legs, the tendency to stall on a given surface decreases, but the tendency for ground interference increases. These same trends were observed when the rolling resistance of the rolling surface was decreased while keeping a constant leg design. So, in a target environment with a higher rolling resistance, a leg design with more mass set out at the tip will tend to roll without stall, but a controller incorporating dynamic ranges with a lower limiting velocity Ω_L will need to be employed to avoid ground interference.

The experimentally validated mathematical model for the cylindrical TRREx presented in this paper could also be applied to study actuated rolling performance by defining performance parameters. One example performance parameter that captures both stall tendency and ground interference tendency is the peak velocity achieved before the second actuation. This is an indicator of starting acceleration and (from Fig. 14, Fig. 15 and Fig. 17) increases from $20^\circ/\text{s}$ to $50^\circ/\text{s}$ to $65^\circ/\text{s}$ as we go from leg design A to B to C, respectively, on Surface 2. Another interesting performance parameter that can be found, by letting the simulations run until a steady state is observed, is the maximum steady state velocity that is attainable by the system on a given surface.

4.3. Discussion on deviations between model and experiments

Although the simulation results exhibit a good match with experimental data, the match is not exact. The causes of the differences between the two can be divided up into two main categories: (1) deviations of the mathematical model from the true response of the system due to inaccurate modeling assumptions, and (2) deviations of the mathematical model from the true response due to experimental errors. Some modeling assumptions that are likely to have introduced a deviation are due to the fact that the movements of the parts of the linear motor were ignored, and the motors were assumed to exactly generate the desired motion of the arms. Inaccuracies could also be due to the relatively simple friction and rolling resistance models used. Additional deviations could be due to inaccurate estimation of the physical parameters (both design and environmental) and inaccuracies which were introduced during fabrication.

5. Conclusions

A novel planetary exploration rover, called the Transforming Roving-Rolling Explorer (TRREx), designed to navigate rugged terrain with steep slopes, was described. A mathematical model that captured the 'actuated rolling' dynamics of a cylindrical version of the TRREx was developed using a Newton-Euler approach. The construction and software development of a physical prototype for the purpose of model validation was presented. Results generated by the mathematical model were compared with data acquired during experimental runs using the prototype. The comparison was done for several different configurations on two different surfaces, and in each case good correspondence was observed between simulation results and experimental data. The good agreement between the results predicted by the dynamic model and experimental results indicates that the model can be used to predict the behavior of the actual physical system, and thus can be used to investigate the capabilities and limitations of actuated rolling of a cylindrical TRREx. While this paper concerns a cylindrical version of the TRREx, insight gained from this study should aid in the design, fabrication, and control optimization of a Spherical TRREx.

Acknowledgements

We gratefully acknowledge support from the NASA Innovative Advanced Concepts Program through NASA Grant No. NNX11AR26G, and from the North Carolina Space Grant Consortium.

References

- [1] D. McCleese, R. Greeley, G. MacPherson, Science planning for exploring mars, JPL Publ. (2001) 01–07.
- [2] H.J. Eisen, C.W. Buck, G.R. Gillis-Smith, Mechanical design of the Mars Pathfinder mission, in: Proceedings of the 7th European Space Mechanisms and Tribology Symposium, 410, pp. 293, 1997.
- [3] R.A. Lindemann, D.B. Bickler, B.D. Harrington, Mars exploration Rover mobility development, Robot. Autom. Mag. IEEE 13 (2) (2006) 19–26.
- [4] D.P. Miller, T. Lee, High-speed traversal of rough terrain using a rocker-bogie mobility system, Space (2002).
- [5] M. Mann, Z. Shiller, Dynamic stability of a rocker bogie vehicle: longitudinal motion, in: Proceedings of 2005 IEEE International Conference on Robotics and Automation (ICRA), Vols 1–4, pp. 861–866, 2005.
- [6] J.P. Grotzinger, J. Crisp, A.R. Vasavada, Mars science laboratory mission and science investigation, Space Sci. Rev. 170 (1–4) (2012) 5–56.
- [7] R.A. Lindemann, C.J. Voorhees, Mars Exploration Rover mobility assembly design, test and performance, in: Proceedings of 2005 IEEE International Conference on Systems, Man and Cybernetics, 1, pp. 450–455, 2005.
- [8] ESA, Perspective view of the Melas Chasma, (http://www.esa.int/spaceinimages/Images/2010/10/Perspective_view_of_the_Melas_Chasma2).
- [9] L.E. Edwin, A.P. Mazzoleni, A.E. Hartl, Dynamic modeling and mobility analysis of the Transforming Roving-Rolling Explorer (TRREx) as it traverses rugged Martian terrain, Acta Astronaut. 120 (2016) 103–120 (March–April 2016).
- [10] J. Denhart, T. Gemmer, L. Edwin, Assessing Reconfigurable Design for a Chaotic Objective in a Mars Exploration Rover, September 17–19, AIAA 2012–5561, 2012.
- [11] L.E. Edwin, J.D. Denhart, T.R. Gemmer, Performance analysis and technical feasibility assessment of a transforming roving-rolling explorer rover for mars exploration, ASME Trans.: J. Mech. Des. 136 (7) (2014) 071010.
- [12] Z. Deng, M. Hu, H. Gao, Mobile system of a six-wheeled lunar rover and dynamic modeling of its steering system, China Machine Press, Beijing; No 1 Nanli Baiwanzhuang, Beijing, Peoples R China, 2004, p. 1571.
- [13] R. Siegwart, P. Lamon, T. Estier, Innovative design for wheeled locomotion in rough terrain, Robot. Auton. Syst. 40 (2–3) (2002) 151–162.
- [14] C. Grand, F. Benamar, F. Plumet, Stability and traction optimization of a reconfigurable wheel-legged robot, Int. J. Robot. Res. 23 (10–11) (2004) 1041–1058.
- [15] G. Freitas, G. Gleizer, F. Lizarralde, Kinematic reconfigurability control for an environmental mobile robot operating in the Amazon rain forest, J. Field Robot. 27 (2) (2010) 197–216.
- [16] C. Grand, F. Benamar, F. Plumet, Motion kinematics analysis of wheeled-legged rover over 3D surface with posture adaptation, Mech. Mach. Theory 45 (3) (2010) 477–495.
- [17] C.C. Phipps, B.E. Shores, M.A. Minor, Design and quasi-static locomotion analysis of the rolling disk biped hybrid robot, IEEE Trans. Robot. 24 (6) (2008) 1302–1314.
- [18] E. Rohmer, G. Reina, K. Yoshida, Dynamic simulation-based action planner for a reconfigurable hybrid leg-wheel planetary exploration rover, Adv. Robot. 24 (8–9) (2010) 1219–1238.
- [19] S. Bhattacharya, S. Agrawal, Spherical rolling robot: a design and motion planning studies, IEEE Trans. Robot. Autom. 16 (6) (2000) 835–839.
- [20] H. Brown, Y. Xu, A Single-Wheel, Gyroscopically Stabilized Robot, 1996 IEEE International Conference on Robotics and Automation, Proceedings, Vols 1–4, pp. 3658–3663, 1996.
- [21] A. Halme, T. Schonberg, Y. Wang, Motion control of a spherical mobile robot, IEEE AMC'96-MIE, , 1996 in: Proceedings of the 4th International Workshop, New York; 345 E 47th St, New York, NY 10017, pp. 264, 1996.
- [22] S. Mahboubi, M.M.S. Fakhrabadi, A. Ghanbari, Design and Implementation of a Novel Spherical Mobile Robot 71 (1) (2013) 43–64.
- [23] G. Shu, Q. Zhan, Y. Cai, Motion Control of Spherical Robot Based on Conservation of Angular Momentum, IEEE, New York; 345 E 47th St, New York, NY 10017 USA, pp. 604, 2009.
- [24] Y. Sugiyama, S. Hirai, Crawling and jumping by a deformable robot, Int. J. Robot. Res. 25 (5–6) (2006) 603–620.
- [25] Q. Zhan, T. Zhou, M. Chen, Dynamic trajectory planning of a spherical mobile robot, IEEE, New York; 345 E 47th St, New York NY 10017 USA, pp. 587, 2006.
- [26] F. Tomik, S. Nudehi, L.L. Flynn, Design, fabrication and control of spherobot: a spherical mobile robot, J. Intell. Robot. Syst. 67 (2) (2012) 117–131.
- [27] L. Meirovitch, Methods of analytical dynamics, Dover, Mineola, N.Y., 2003.
- [28] T.R. Kane, D.A. Levinson, Dynamics, theory and applications, McGraw Hill, 1985.
- [35] L.E. Edwin, Transforming Roving-Rolling Explorer (TRREx) for Planetary Exploration (Ph.D. Dissertation), North Carolina State University, 2014.
- [36] J. Uicker Jr, G. Pennock, J. Shigley, Theory Mach. Mech. (2003).
- [37] MATLAB version 8.1.0.604 (R2013a), The MathWorks Inc., 2013, Natick, Massachusetts.
- [38] NI sbRIO-9611 (<http://sine.ni.com/nips/cds/view/p/lang/en/nid/205893>).
- [39] National Instruments, LabVIEW 2013, (<http://www.ni.com/labview/>).
- [40] P. Kumar, D. Sarkar, S. Gupta, Rolling resistance of elastic wheels on flat surfaces, Wear 126 (2) (1988) 117–129.
- [41] K.W. Li, W. Chang, T.B. Leamon, Floor slipperiness measurement: friction coefficient, roughness of floors, and subjective perception under spillage conditions, Saf. Sci. 42 (6) (2004) 547–565.
- [42] H. Ikuko, G. Toshihiro, Slipperiness and coefficient of friction on the carpets, J. Text. Eng. 47 (2) (2001) 53–58.
- [43] J.M. Miller, “Slippery” work surfaces: towards a performance definition and quantitative coefficient of friction criteria, J. Saf. Res. 14 (4) (1984) 145–158.